ARTICLE IN PRESS
EPSL:13574

Earth and Planetary Science Letters ••• (••••) •••–•••

Contents lists available at ScienceDirect

Earth and Planetary Science Letters

www.elsevier.com/locate/epsl

Kinetics of the olivine–ringwoodite transformation and seismic attenuation in the Earth's mantle transition zone

J.P. Perrillat [a,*], M. Chollet [a,b], S. Durand [a], B. van de Moortèle [a,1], F. Chambat [a], M. Mezouar [c], I. Daniel [a]

[a] Laboratoire de Géologie de Lyon, UMR5276, Université Claude Bernard Lyon 1, CNRS, ENS Lyon, 69622 Villeurbanne, France
[b] Laboratory for Nuclear Materials, Paul Scherrer Institut, 5232 Villigen, Switzerland
[c] European Synchrotron Radiation Facility, 38000 Grenoble, France

ARTICLE INFO

Article history:
Received 6 July 2015
Received in revised form 9 October 2015
Accepted 10 November 2015
Available online xxxx
Editor: J. Brodholt

This paper is dedicated to the memory of Bertrand van de Moortèle

Keywords:
olivine
ringwoodite
kinetics
high-pressure
seismic attenuation
Earth's mantle

ABSTRACT

In regions of the mantle where multi-phases coexist like at the olivine–wadsleyite–ringwoodite transitions, the stress induced by the seismic waves may drive a mineralogical reaction between the low to high pressure phases, a possible source of dissipation. In such a situation, the amount of attenuation critically depends on the timescale for the phase transformations to reach equilibrium relative to the period of the seismic wave. Here we report synchrotron-based measurements of the kinetics of the olivine to ringwoodite transformation at pressure-temperature conditions of the co-stability loop, for iron-rich olivine compositions. Both microstructural and kinetic data suggest that the transformation rates are controlled by growth processes after the early saturation of nucleation sites along olivine grain boundaries. Transformation-time data show an increase of reaction rates with temperature and iron content, and have been fitted to a rate equation for interface-controlled transformation: $G = k_0 \cdot T \cdot \exp[n \cdot X_{\mathrm{Fa}}] \cdot \exp[-(\Delta H_a + PV^*)/RT] \times [1 - \exp(\Delta G_r/RT)]$, where X_{Fa} is the fayalite fraction, the exponential factor $n = 9.7$, $\ln k_0 = -9.1\ \mathrm{m\,s^{-1}}$. X_{Fa}^{-1} and $\Delta H_a = 199$ kJ/mol, assuming $V^* = 0\ \mathrm{cm^3/mol}$. Including these new kinetic results in a micro-mechanical model of a two-phase loop (Ricard et al., 2009), we predict Q_K^{-1} and Q_μ^{-1} significantly higher than the PREM values for both body waves and normal modes. This attests that the olivine–wadsleyite transition can significantly contribute to the attenuation of the Earth's mantle transition zone.

© 2015 Elsevier B.V. All rights reserved.

1. Introduction

Current knowledge of the structure and composition of the Earth's mantle primarily comes from studies of elastic wave speeds. Based on travel times of body waves, dispersion of surface waves, and splitting of free oscillations, seismologists estimate variations in elastic wave speeds within the Earth's interior. However, the Earth's mantle is not a purely elastic solid and the attenuation of seismic waves in the mantle shows that relaxation occurs even at seismic frequencies (e.g. Romanowicz and Mitchell, 2007). The physical mechanisms proposed to explain the observed attenuation include motion of dislocations, grain boundary sliding, rearrangement of point defects, and phase transformations that may have a significant contribution (see Jackson, 2007, for a review). Most phase transformations in the mantle occur across multi-phase regions. When a seismic wave propagates through a zone where two or more phases coexist, the associated stress oscillations disrupt locally the thermodynamic equilibrium. Since the phase change is not instantaneous, the re-equilibration is delayed after the perturbation induced by the wave. As a result, the seismic wave undergoes attenuation and dispersion (e.g. de Groot and Mazur, 1984). For instance, this may occur when olivine transforms to its high-pressure polymorphs, wadsleyite and ringwoodite, at 410 and 520 km depth, respectively. Those transitions are first order character, they are associated to substantial volume decrease (i.e. ∼6% for the olivine–wadsleyite and ∼2% for the wadsleyite–ringwoodite reaction; Akaogi et al., 1989), and have finite widths owing to the partitioning of iron and magnesium between coexisting low- and high-pressure phases. Ricard et al. (2009) developed a thermomechanical model of the equilibrium loop of a divariant solid–solid phase transformation involving both bulk and shear deformations, and showed that the resulting medium has a standard linear solid viscoelastic behaviour whose attenuation mainly depends upon the kinetics of the phase change.

* Corresponding author. Tel.: +33 472 446 241.
E-mail address: jean-philippe.perrillat@univ-lyon1.fr (J.P. Perrillat).
[1] Deceased.

http://dx.doi.org/10.1016/j.epsl.2015.11.013
0012-821X/© 2015 Elsevier B.V. All rights reserved.

Please cite this article in press as: Perrillat, J.P., et al. Kinetics of the olivine–ringwoodite transformation and seismic attenuation in the Earth's mantle transition zone. Earth Planet. Sci. Lett. (2015), http://dx.doi.org/10.1016/j.epsl.2015.11.013

Table 1
Chemical composition of starting materials from EDS measurements (atomic percent).

	Mg	Si	Fe	O	X_{Fe}
Fa52	9.89 (0.4)	13.97 (0.18)	19.15 (0.55)	56.99 (0.09)	0.52 (0.0203)
Fa66	13.93 (0.67)	14.10 (0.28)	14.93 (0.62)	57.05 (0.14)	0.66 (0.0105)

X_{Fe} corresponds to the iron content (i.e. proportion of the fayalite end-member) of the olivine samples. Analysis were performed on a JEOL 840 microscope at the CLYM laboratory (Lyon, France). Numbers in parentheses indicate one standard deviation from six successive analyses.

Because of their relevance to mantle petrology, olivine high-pressure transitions have received considerable attention in terms of phase diagram and transformation mechanisms. Although critical to predict the attenuation of seismic waves, available information on phase kinetics from laboratory experiments is however limited. Most of the available kinetic data focused on Mg or Fe end-member of the olivine solid solution, or on San Carlos olivine typical of the upper mantle (Furnish and Basset, 1983; Yagi et al., 1987; Rubie and Ross, 1994; Kubo et al., 1998a; Kubo et al., 1998b; Liu et al., 1998; Kerschhofer et al., 2000; Mosenfelder et al., 2001; Hosoya et al., 2005; Diedrich et al., 2009; Perrillat et al., 2013; Du Frane et al., 2013). For the San Carlos composition Fa10, the thickness of the olivine (α)–wadsleyite (β) coexistence loop is limited to 0.4(1) GPa at mantle temperature, so that most kinetic studies have been performed in the stability field of either wadsleyite (β) or ringwoodite (γ), rather than in the coexistence loop. However, transformation rates are governed by nucleation and growth processes that might significantly differ in the loop as both phases already coexist.

The present work reports kinetic measurements within the co-stability loop of olivine and ringwoodite for Fa52 and Fa66 compositions. Such iron-rich compositions were chosen since the α–γ transition occurs at lower pressure and over a binary loop of 3–4 GPa at 900–1600 K (Akaogi et al., 1989). Time-resolved XRD patterns reveal a short amorphization step of olivine at the onset of transformation that we relate to the pseudo-martensitic reaction mechanism and the diffusion of cations to achieve equilibrium phase compositions (Furnish and Basset, 1983; Raterron et al., 2002; Perrillat et al., 2013). Kinetic parameters derived from the transformation-time data show an increase of reaction rates with the iron content, but have the same temperature dependence as those previously obtained on Fa10 composition. We finally use these new kinetic data in the micro-mechanical model of Ricard et al. (2009) to assess the contribution of α–β transition to the seismic attenuation of the Earth's mantle transition zone.

2. Materials and methods

2.1. Starting materials

Olivine powders with two different Fe-content, $X_{Fe} = 0.52$ (Fa52) and $X_{Fe} = 0.66$ (Fa66) were synthesized under controlled oxygen fugacity at 10^{-10} atm at high temperature. Stoechiometric amounts of MgO, SiO_2 and Fe_2O_3 powders were mixed and loaded in an alumina crucible into a vertical furnace (at CRPG-CNRS, Nancy, France). Oxygen fugacity was controlled by a CO–CO_2 mixture. Samples were heated during 20 h at 1250 °C, close to the solidus of Fe-rich olivine. Then, samples were quenched in the ambient atmosphere, which leaded to the formation of hematite on the rims of the sample. Consequently, we picked out only the cores of pellets free of hematite which were then ground in an agate mortar. The powder purity was checked by X-ray diffraction to be entirely olivine, and the homogeneity of chemical composition was controlled by EDS measurements (Table 1).

2.2. Experimental method

Angle-dispersive X-ray diffraction measurements were performed in a Paris–Edinburgh press at the ID27 high-pressure beamline of the European Synchrotron Radiation Facility (ESRF, Grenoble, France). Monochromatic X-rays of 0.6199 Å wavelength (20 keV, Mo-edge) were focused by two mirrors in KB geometry into a spot of 15 × 15 µm on the sample. The contribution of the sample environment to the signal was spatially filtered by Soller slits (Morard et al., 2011). Diffracted X-rays were collected with a MARCCD® detector over a 2θ range of 4–25° and integrated using Fit2D. Thanks to the bright focused X-ray beam, exposure times were reduced to 5 s and a time resolution of 23 s between each spectra has been achieved in some experiments. Time resolution is chiefly limited by the mechanical rotation of the Soller's slits to cover the whole 2θ range. This high time resolution is mandatory to investigate the transient phenomena that occurred in the very first steps of the transformation.

Powders of Fa52 or Fa66 olivine were loaded in MgO containers. The heater consisted of two $LaCrO_3$ ceramic disks on both sides of the sample and in electrical contact trough two rhenium strips (50 µm thick) oriented parallel to the X-ray beam. The whole assembly detailed by Morard et al. (2007) is contained in a biconical boron epoxy gasket of outer diameter of 5 mm and placed between sintered diamond anvils. The maximal thermal gradient across the sample was estimated from numerical simulations to be lower than 80 K at 873 K (see Fig. 1 in Perrillat et al., 2013). Pressure and temperature conditions were determined according to the cross calibration method using the equations of state of Takemura (2001) and Yamamoto et al. (1987) for Au and NaCl, respectively. For this purpose, an Au–NaCl powder (1:4 weight proportions) was packed on one side of the sample, against the MgO container. Diffraction spectra were acquired periodically on the sample and P–T calibrants, and cell parameters of NaCl and Au were determined by a LeBail refinement using the GSAS software (Larson and Von Dreele, 2004). Uncertainties on P and T depend on both the error in fitting the diffraction lines and the uncertainty on the thermoelastic parameters of the calibrants which only leads to a constant shift of the P–T conditions. Therefore we only take into account the ±0.002 Å error on the d-spacing of the Au and NaCl diffraction lines. The precision on P and T is in all cases better than ±0.5 GPa and ±70 K.

Samples were first cold compressed up to ca. 8 GPa, and annealed within the olivine stability field at ca. 700 K over 1–2 h. The sharpening of olivine diffraction lines during the annealing time and the lack of lattice preferred orientation on the 2D-XRD images (i.e. no variation of line intensities with the ψ azimuthal angle) both argue for strain relaxation within the sample, consistent with the <0.05 GPa amount of deviatoric stress estimated from the method of Singh and Kennedy (1974) on NaCl diffraction lines. After this hot-pressing stage, pressure was increased to the target value either within the divariant loop or in the ringwoodite stability field (Fig. 1). Temperature was then rapidly increased at a rate of 15–35 K/min to reach the target temperature within 5–8 min. Diffraction patterns were recorded during the temperature ramp and then under isothermal conditions to monitor the extent of transformation to ringwoodite as a function of time. Tem-

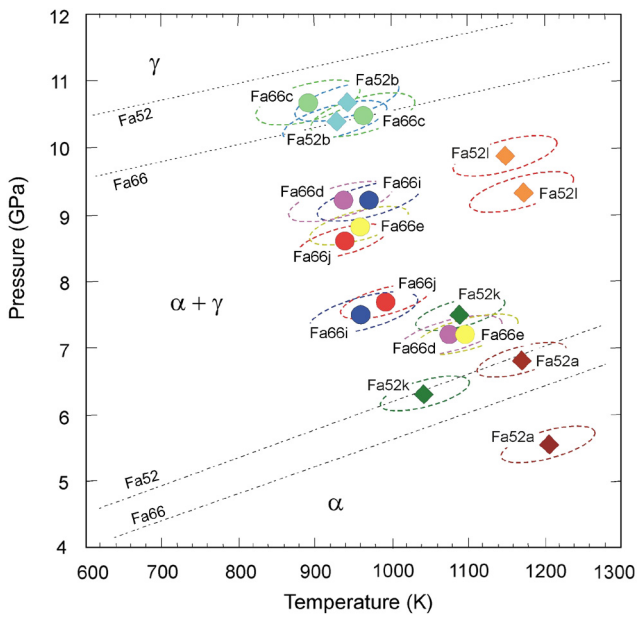

Fig. 1. Pressure–temperature diagram showing the experimental P–T conditions with error ellipses, and the phase relations between olivine and ringwoodite for Fa52 (diamonds) and Fa66 (circles) compositions from Matas (1999). The P–T conditions at the onset and end of transformation for each experimental charges are represented with symbols of identical colour (see the online version for colours). P and T were determined from the diffraction lines of Au and NaCl using a cross-calibration of their PVT equation of state (see section 2.2 for details).

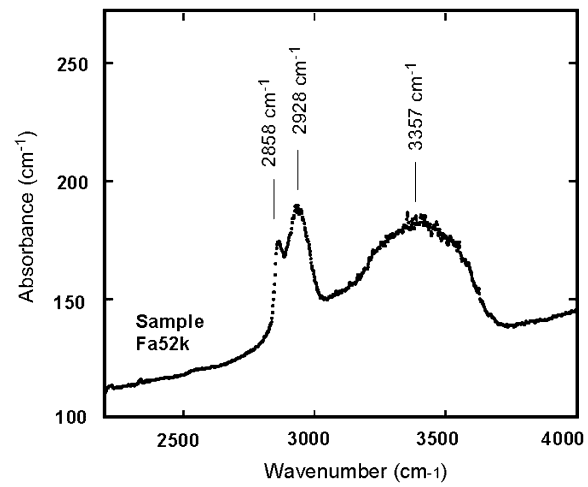

Fig. 2. Unpolarized IR spectrum of recovered sample Fa52k in the region of the OH stretching modes. All the samples exhibit a broad absorption band in the range 3000 to 4000 cm^{-1}, attributable to the presence of molecular H_2O at grain boundaries. The hydroxyl content is calculated from the integrated area of this broad absorption band after background baseline correction and thickness normalization using the general calibration of Libowitzky and Rossman (1997). The bands located near 2900 cm^{-1} are characteristic of C–H bending of the epoxy glue and are disregarded for the determination of OH contents.

perature and pressure were held constant by imposing a small drift on the furnace power set point and the applied oil pressure, respectively. However, for the fastest reactions, it was not possible to compensate for the volume decrease during the reaction. That led to a pressure drop of 1–2 GPa during the reaction (Fig. 1). Finally, when phase proportions reached a steady-state, equilibrium in the divariant loop was assumed, samples were quenched in temperature and pressure was subsequently slowly released.

All recovered samples were observed by back-scattering electron images, obtained with a JEOL 840 scanning electron microscope (SEM) at the CLYM laboratory (Lyon, France). Microstructural observations allowed characterizing the different stages of the reaction progress and nucleation-growth mechanism. Considering the potentially strong catalytic effects of even small amount of H_2O in the sample charges, water content of the samples was determined from Fourier transform infrared spectroscopy (FTIR) using a Vertex 70 Bruker spectrometer coupled to a Hyperion microscope (at Institut de Planétologie et Astrophysique, Grenoble, France). Details of FTIR measurements are described elsewhere (Perrillat et al., 2013). The OH content of the samples, as calculated using the calibration by Libowitzky and Rossman (1997), varies from 154 to 603 wt.ppm H_2O with an average value of 436 wt.ppm H_2O (Fig. 2).

3. Results and discussion

3.1. Mechanisms of transformation within the binary olivine–ringwoodite loop

Nine sets of kinetic data have been recorded over the 6.8–10.7 GPa and 891–1172 K P–T range (Fig. 1 and Table 2). A typical sequence of diffraction spectra is displayed in Fig. 3b for sample Fa66c. The transformation of olivine into ringwoodite is evidenced by the appearance and the continuous increase of ringwoodite diffraction lines at the expense of olivine. Transformation proceeds until it reaches a steady state, i.e. the relative proportion

Table 2
Experimental conditions and estimated values of grain-boundary nucleation and growth rates.

	V_{Au} (Å^3)	V_{NaCl} (Å^3)	Pressure (GPa)	Temperature (K)	Free energy change ΔG_r (J/mol)	Final proportion of ringwoodite (%)		Nucleation rate (m^{-2}/s)	Growth rate (m/s)
						From XRD data	From SEM images		
Fa52a	67.61	153.89	6.8	1172	−330	6	9	–	1.57 (0.75) × 10^{-09}
Fa52b	65.60	143.92	10.7	942	−808	49	61	–	1.13 (0.06) × 10^{-10}
Fa52k	67.12	152.18	7.5	1088	−462	14	6	–	3.00 (0.48) × 10^{-09}
Fa52l	66.37	144.87	9.9	1143	−363	22	14	–	1.14 (0.12) × 10^{-09}
Fa66c	65.46	143.86	10.7	891	−1353	82	75	1.95 (0.89) × 10^{12}	2.06 (0.23) × 10^{-10}
Fa66d	66.12	147.48	9.2	940	−3069	62	59	–	1.06 (0.28) × 10^{-09}
Fa66e	66.29	148.58	8.8	959	−2227	45	–	–	2.76 (0.46) × 10^{-09}
Fa66i	66.18	147.46	9.2	971	−2706	41	35	–	5.51 (1.13) × 10^{-09}
Fa66j	66.32	149.07	8.6	939	−1584	48	–	–	5.15 (0.31) × 10^{-10}

Pressure and temperature conditions were determined from the diffraction lines of Au and NaCl using the PVT equations of state of Takemura (2001) and Yamamoto et al. (1987), respectively.
The free energy change ΔG_r at P–T was calculated from the thermodynamic data of Akaogi et al. (1989) and Jacobs and de Jong (2005).
The final proportion of ringwoodite was estimated (1) by Rietveld refinement of XRD data, and (2) by image analysis of SEM pictures of the quenched products. In this last case, the iron-rich ringwoodite was distinguished from olivine by its higher grey levels, and the "Threshold" tools of the ImageJ® software were used for the segmentation/quantification analysis.
Nucleation and growth rates were obtained by a fit of the experimental $\xi(t)$ data to Cahn's equation (1). Estimated uncertainties are listed in parentheses. When a solution for N was not achieved, an arbitrary high value of $N = 10^{14}$ m^{-2}/s was set.

Please cite this article in press as: Perrillat, J.P., et al. Kinetics of the olivine–ringwoodite transformation and seismic attenuation in the Earth's mantle transition zone. Earth Planet. Sci. Lett. (2015), http://dx.doi.org/10.1016/j.epsl.2015.11.013

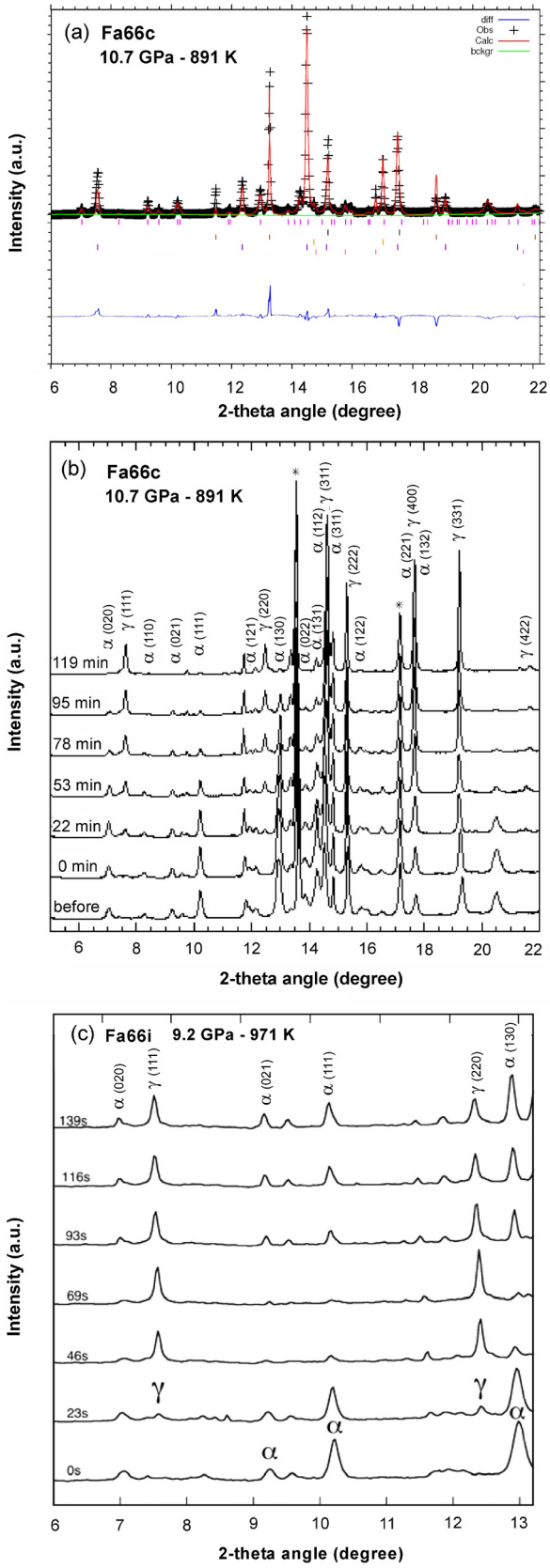

Fig. 3. (a) Example of a Rietveld refinement performed with GSAS on an XRD pattern from sample Fa66c; (b) time series of XRD patterns acquired at 10.7 GPa–891 K showing the transformation of olivine into ringwoodite (sample Fa66c); (c) and selected patterns at the onset of reaction highlighting the disappearance and re-appearance of olivine diffraction peaks (sample Fa66i at 9.2 GPa–971 K). Diffraction lines are labelled as α(hkl) and γ(hkl) for olivine and ringwoodite, respectively. Asterisks indicate the position in 2θ of MgO lines of the container.

of α and γ phases defined at equilibrium in the binary loop, after ~115 min at 10.7 GPa–891 K. The sequence recorded on sample Fa66i (Fig. 3c), thanks to a high time resolution of 23 s, depicts the early stages of the reaction. It clearly shows that the (020), (021), (111) and (130) diffraction lines of olivine decrease in intensity and disappear during the first tens of seconds of the transition, after ringwoodite has nucleated. Since the others intense peaks of olivine, (112), (311), (221) and (132), are superposed with the intense ones of ringwoodite, (311) and (400), we cannot clearly state if the whole pattern of olivine disappeared or not. In the mean time, ringwoodite diffraction lines never stop growing. With increasing time ($t = 93$ s) the diffraction lines of olivine re-appear and increase again in intensity. A similar behaviour has been observed in run Fa66d, where diffraction lines of olivine disappeared after $t = 4$ min, and grew again at $t = 7$ min. Hence, the very first steps of the reaction are characterized by a loss of the coherence of the diffraction signal of olivine. It is consistent with an amorphization of olivine, at least at the characteristic length scale of the X-rays wavelength, i.e. 0.6 Å. To our best knowledge, this is the first report of such a transient phenomenon. We believe it systematically occurs during the transformation, but its observation requires a high time-resolution that can only be achieved using a synchrotron X-ray source and fast CCD detectors.

We interpret the amorphization of olivine at the onset of transformation as the result of the inferred pseudo-martensitic reaction. Indeed, the pseudo-martensitic mechanism involves two stages: a shear-induced re-arrangement of the *hcp* oxygen sub-lattice of olivine into the *fcc* configuration in ringwoodite, followed by a re-ordering of the cations by diffusion (e.g. Furnish and Basset, 1983; Chen et al., 2001). This mechanism operates under hydrostatic and near-equilibrium conditions, and is driven by the shear stress generated by the volume change of the transformation itself (Raterron et al., 2002). This model involves the early development of a high density of defects in the olivine that further act as nucleation sites for ringwoodite. Staking faults, twins and dislocations in partially transformed olivine samples have been reported in many previous experimental works (e.g. Green and Burnley, 1989; Guyot et al., 1991; Brearley et al., 1992; Kerschhofer et al., 1996; Raterron et al., 2002; Smyth et al., 2012). We therefore relate the disappearance of olivine diffraction lines to the built up of defects that alter the periodicity of the olivine crystal, leading to transient amorphization.

Microstructural observations of recovered samples support this reaction mechanism. SEM images of samples with limited transformation (Fig. 4a, sample Fa52a with 6% of transformation) indicate that ringwoodite nucleated at the olivine grain or sub-grain boundaries. This is consistent with the proposed stress-induced mechanism of reaction, since the maximum densities of defects should be concentrated at grain boundaries (e.g. Poirier, 1981; Mosenfelder et al., 2001). This nucleation stage is followed by the growth of ringwoodite grains enriched in iron compared to the original olivine (light grey areas on SEM images Fig. 4b). The evolution of the sample microstructures as a function of the extent of transformation is consistent with nucleation at grain boundary and interface-controlled growth as reported in early works on the olivine–ringwoodite transformation (Brearley et al., 1992; Mosenfelder et al., 2001; Kubo et al., 2004; Smyth et al., 2012). While the initial grain size of olivine after annealing is about 7 ± 2 µm, the ringwoodite grain size is limited to ca. 2 µm after transformation (Figs. 4b and 4c). This evidences an important grain size reduction of ca. 70% associated to the olivine–ringwoodite transformation. Finally, SEM images of run Fa66c (Fig. 4c), transformed up to 80%, still displayed chemically heterogeneous olivine grains. The initial olivine crystals thus fell to fully re-equilibrate with the ringwoodite composition, indicating that cations interdiffusion is the slowest process of the reaction.

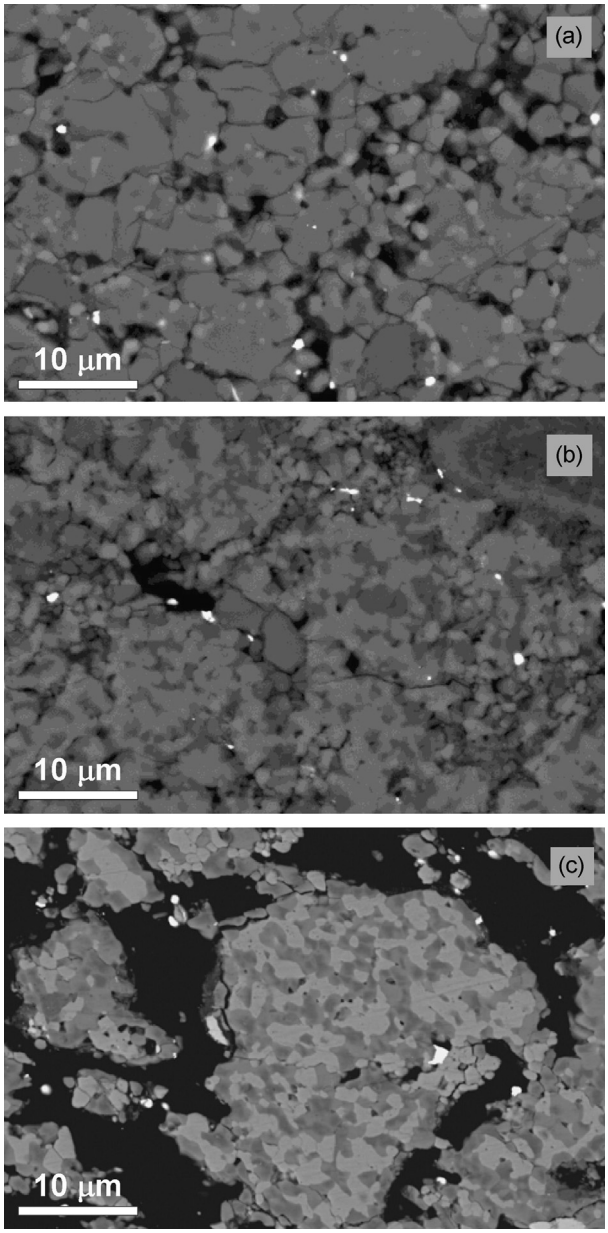

Fig. 4. Electron backscattered images showing characteristic microtextures of recovered samples (a) Fa52a, (b) Fa52b and (c) Fa66c, ordered by extent of transformation from 6, 49 to 82% respectively. Ringwoodite (in light grey) forms at grain boundaries of olivine (in dark grey), and then grows at grains interfaces. The transformation involves cationic-readjustment diffusion processes as evidenced by the presence of chemically heterogeneous olivine grains on image (c). Bright dots are gold particles used for P–T calibration. Black areas correspond to cracks and former NaCl grains dissolved while preparing the polished sections.

3.2. Kinetics analysis and transformation rates

Rietveld refinements of time-series XRD patterns using the GSAS package (Fig. 3a, Larson and Von Dreele, 2004) provide the evolution of the relative amount of olivine and ringwoodite as a function of time. The variations in iron content of α and γ phases within the binary loop were not considered in the Rietveld procedure, as we assumed a constant X_{Fe} for olivine and ringwoodite during the transformation. The relative error in mineral proportion is estimated to be ±10% from the scattering of phase fractions obtained from repeated Rietveld refinements of a same spectrum. The transformed weight fraction is reported as a function of time for the nine runs in Fig. 5. Steady state of the olivine–ringwoodite transformation is reached within timescales from ten minutes (runs Fa52k and Fa66e) to ca. six hours (run Fa52b). The nine runs reached different olivine–ringwoodite proportions at equilibrium, from 6 wt% of ringwoodite for run Fa52a to 82 wt% for Fa66c, depending on the target P–T conditions within the α–γ binary loop. These final phase proportion of ringwoodite are in broad agreement with those estimated from SEM images of the quenched samples (Table 2). Discrepancies may arise from thin sectioning effects, and from intrinsic differences between electron microscopy that is sensitive to chemistry and X-ray diffraction that probes the crystal structure. For runs Fa66d and Fa66i, the first points of the transformation-time curves are affected by the amorphization of olivine, so that the proportion of ringwoodite is largely overestimated during the first minutes of the reaction. These points were therefore disregarded in the kinetic analysis.

The extent of transformation $\zeta(t)$ is defined as the ratio of ringwoodite's weight fraction produced at time t over the maximal weight fraction of ringwoodite at the end of reaction. It is equal to zero at the beginning of reaction and to one when equilibrium is achieved (Fig. 5). The $\zeta(t)$ data were analyzed using the general rate equation describing a transformation by grain-boundary nucleation and growth mechanisms (Cahn, 1956):

$$\xi(t) = 1 - \exp\left[-2S\int_0^{y'}\{1-\exp(-z)dy\}\right] \quad (1)$$

where

$$z = \pi\int_0^{t-t'} N\left[G^2(t-\tau)^2 - y^2\right]d\tau \quad (2)$$

and N is the nucleation rate, G is the growth rate of the product phase, $y' = Gt$ is the growth distance after time t, τ is the time at which a nucleus forms, and t' is the time necessary for a nucleus to grow to radius y. S is the grain boundary area that was approximated by $S = 3.35/d$, with d the mean grain size estimated by SEM on quenched samples. Growth rates (G), estimated by a fit of the experimental $\xi(t)$ data to equation (1), vary from 1.13×10^{-10} m s^{-1} to 5.51×10^{-9} m s^{-1} (Fig. 5 and Table 2). In most runs, the solution for N did not converge because of extremely rapid nucleation; and only one high value of $N = 1.95 \times 10^{12}$ m^{-2} s^{-1} could be obtained, for run Fa66c. Consequently, other N were taken as high as 10^{14} m^{-2} s^{-1}. Fig. 5 shows that the fits to $\xi(t)$ data do not deviate significantly from the Cahn's relation, except for run Fa66i. This is an evidence for steady-state growth rates during the transformation and for the absence of grain impingement or transformation stress (Liu et al., 1998) that could potentially decrease the growth rates at the late stages of the reaction. It is in agreement with the conclusion of Liu et al. (1998) that transformation stress is minor when the reactant olivine is fine grained.

Growth rates were analyzed according to the rate equation for interface-controlled transformation (Turnbull, 1956):

$$G = k_0 T\exp\left[-\left(\Delta H_a + PV^*\right)/RT\right] \times \left[1-\exp(\Delta G_r/RT)\right] \quad (3)$$

where k_0 is a rate constant, ΔH_a the activation enthalpy for growth, V^* is the activation volume for growth, R the gas constant and ΔG_r the free energy change of the transformation. The ΔG_r values were calculated from the thermodynamic data of Akaogi et al. (1989) and Jacobs and de Jong (2005), using the proportions and chemistry of α and γ phases at the present run conditions. The activation volume (V^*) describes the pressure dependence of growth rates. A precise determination of V^* relies on the availability of transformation rate data over a large pressure overstep

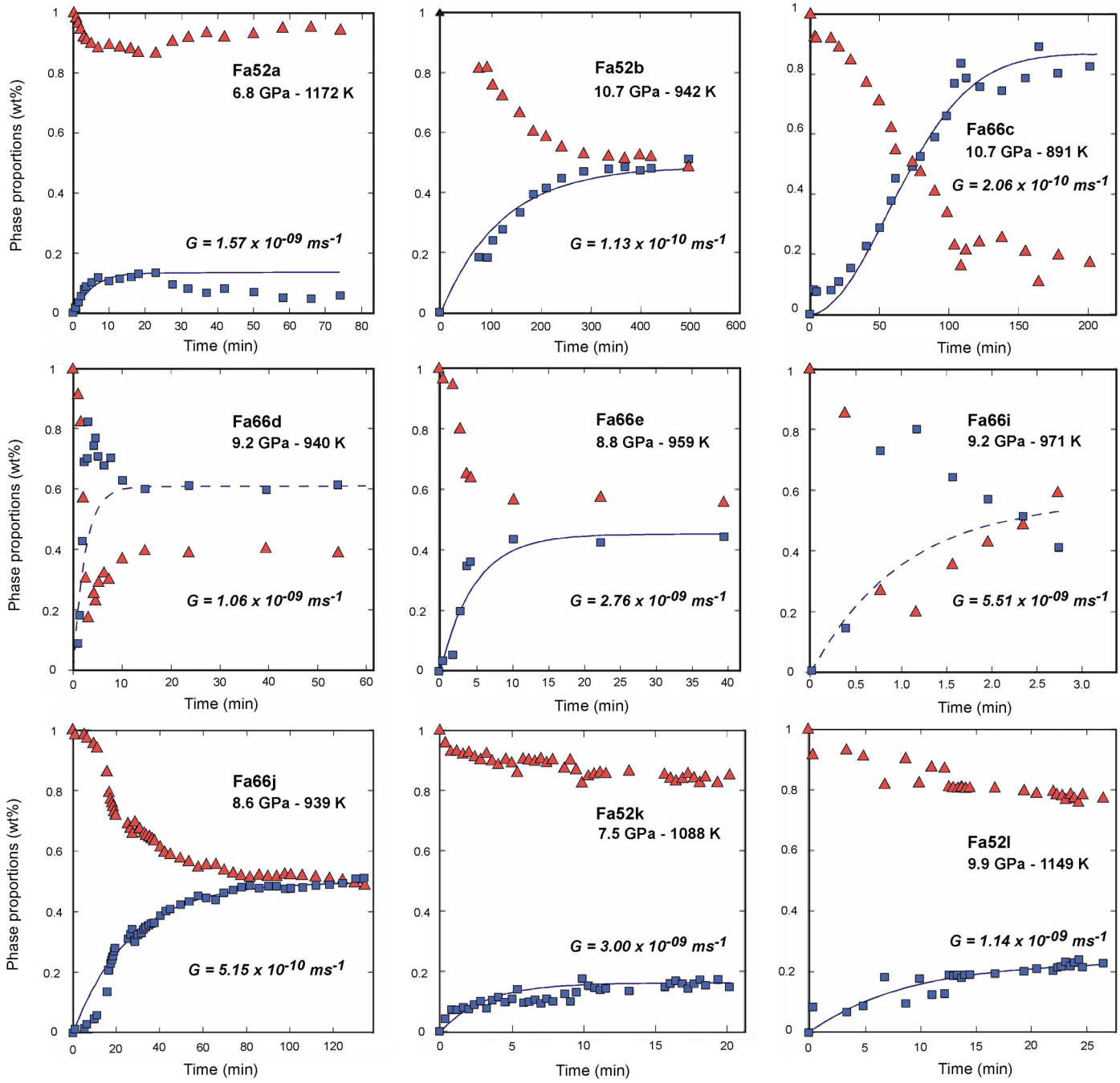

Fig. 5. Evolution of olivine (red triangles) and ringwoodite (blue squares) phase proportions as a function of time at given temperatures and pressures. The solid curves represent best fits of experimental data to the Cahn rate equation (1) with optimized values of growth rates (G). For sample Fa66d and Fa66i, phase proportions at the onset of reaction are affected by the amorphization of olivine, and these first points were therefore disregarded in the fitting procedure (dash lines). See section 3.2 for more details. (For interpretation of the references to colour in this figure legend, the reader is referred to the web version of this article.)

relative to equilibrium conditions. In the present study, we only varied pressure to account for the pressure decrease of the α–γ transition with increasing iron content. The value of V^* would be therefore largely unconstrained, and we preferred to assume $V^* = 0$ cm^3/mol. This assumption is supported by the low activation volume $V^* = 1.7$ (4.5) cm^3/mol determined by Kubo et al. (2004) for the α–β transition in Mg_2SiO_4 and $V^* = 0$ (2) cm^3/mol estimated for the reconstructive growth of γ–Mg_2GeO_4 (Burnley, 1995). Values of k_0 and ΔH_a, for Fa52 and Fa66 starting materials, were estimated from the slope and intercept of a least squares linear fit to the growth rate data on an Arrhenius plot $\ln\{G/T[1 - \exp(-\Delta G_r/RT)]\}$ vs $1000/T$ (Fig. 6a). The best fit yields values of $\ln k_0 = 3.9(8.3)$ m/s/K and $\Delta H_a = 233(69)$ kJ/mol for Fa66 samples, and $\ln k_0 = -9.2(6.1)$ m/s/K and $\Delta H_a = 140(48)$ kJ/mol for Fa52 samples.

The results of the present study are combined with growth rate data of Perrillat et al. (2013) obtained on Fa10 samples, to discuss the temperature and iron dependences on the kinetics (Fig. 6a). The activation enthalpies for runs Fa10, Fa52 and Fa66 are consistent within mutual uncertainties. The lower ΔH_a value for the Fa52 composition is mainly constrained by one experimental point, and thus suffers from a large uncertainty. The similar temperature dependence of growth rates is consistent with a common reaction mechanism for the α–β–γ transformations along the olivine solid solution. We interpret the enhancement of transformation rates from Fa10 to Fa66 by the presence of iron, as the water content of

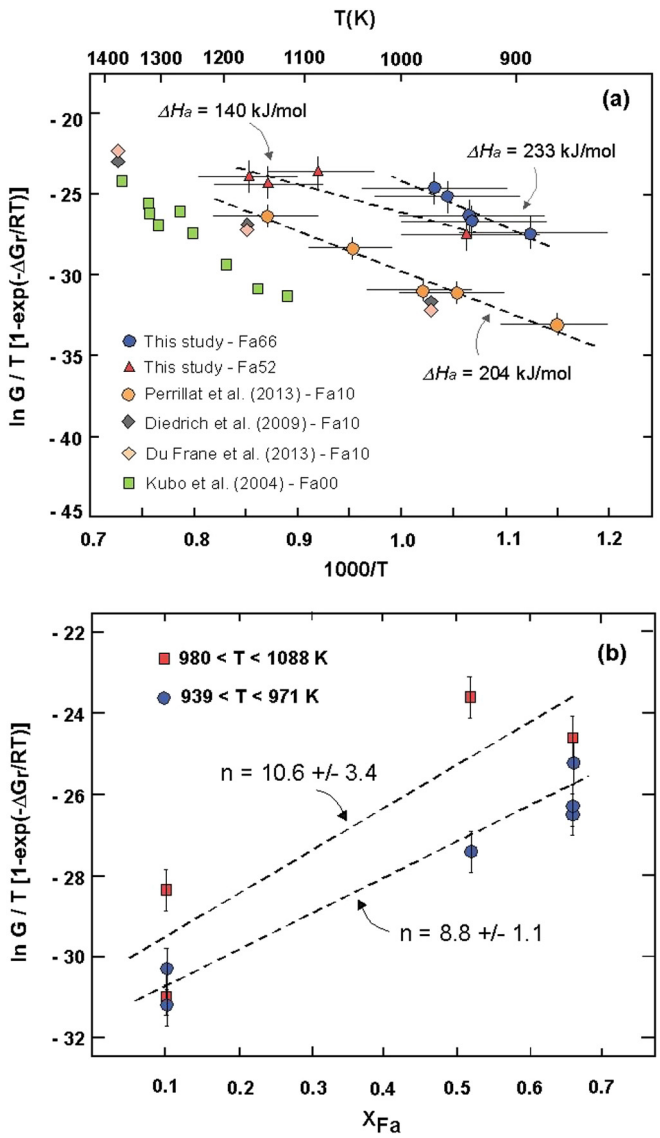

Fig. 6. (a) Temperature dependence of growth rates of ringwoodite for Fa52 and Fa66 compositions, shown as a plot of $\ln G$ against $10^3/T$. Linear fit to the data defines the activation energies for growth of $\Delta H_a = 140$ kJ/mol and $\Delta H_a = 233$ kJ/mol, for Fa52 and Fa66 respectively. Kinetic data for $Mg_{1.8}Fe_{0.2}SiO_4$ – 526 wt.ppm H_2O (Perrillat et al., 2013; orange circles), $Mg_{1.8}Fe_{0.2}SiO_4$ – 360 wt.ppm H_2O (Diedrich et al., 2009; grey diamonds), $Mg_{1.8}Fe_{0.2}SiO_4$ – 75 wt.ppm H_2O (Du Frane et al., 2013; pink diamonds), and synthetic Mg_2SiO_4 (Kubo et al., 2004; green squares) are shown for comparison. (b) Plot of normalized growth rate against iron content for experiments Fa10, Fa52 and Fa66 performed in the temperature range 939–971 K (blue circles) and 980–1088 K (red squares). The linear relation defined by each set of data reveal an exponential dependence on iron content. The exponential factor n is indicated for each temperature data set. (For interpretation of the references to colour in this figure legend, the reader is referred to the web version of this article.)

the samples between Perrillat et al. (2013) and the present study are equivalent at ~500 wt.ppm H_2O. A plot of log- growth rates against the Fa content shows a linear relation, indicative of an exponential dependence. We therefore modified equation (3) to an empirical equation by inserting an exponential dependence on iron content as follows:

$$G = k_0 \cdot T \cdot \exp[n \cdot X_{\mathrm{Fa}}] \cdot \exp\left[-\left(\Delta H_a + PV^*\right)/RT\right] \times \left[1 - \exp(\Delta G_r/RT)\right] \quad (4)$$

where X_{Fa} is the fayalite fraction, and n the exponential factor. The best fit to growth rate data yields $n = 9.7$, $\ln k_0 = -9.1$ m s^{-1}. X_{Fa}^{-1} and $\Delta H_a = 199$ kJ/mol, assuming $V^* = 0$ cm^3/mol. This kinetic dependence on iron concentration might result from the pseudomartensitic reaction mechanism that involves a short-range Fe–Mg interdiffusion. This diffusion process is strongly composition dependent in olivine and its high-pressure polymorphs, with diffusion coefficients increasing with the iron content and decreasing with pressure (see Chakraborty, 2010 for a review). Hence, the lower α–γ transition pressure and the high Fe content would explain the faster kinetics for Fa52 and Fa66 samples. The present kinetic parameters are in agreement with the $\Delta H_a = 237$ kJ/mol reported by Diedrich et al. (2009) on 360 wt.ppm H_2O $Mg_{1.8}Fe_{0.2}SiO_4$ and $\Delta H_a = 207$ kJ/mol reported by Du Frane et al. (2013) on 75 wt.ppm H_2O $Mg_{1.8}Fe_{0.2}SiO_4$. It is however significantly lower than the 391(73) kJ/mol value obtained by Kubo et al. (2004) on pure forsterite samples with 750 wt.ppm H_2O. A lower temperature dependence in iron-bearing samples implies faster transformation rates, which could make great difference at the cold conditions of subducting slabs. Differences in water content of the starting materials cannot account for all the discrepancy between the above studies. Indeed, Du Frane et al. (2013) showed that transformation rates do not strongly depends on the H_2O content, and that the catalytic effect of water is mostly related to hydrolytic weakening of ringwoodite reaction rims by reduction of the elastic strain-energy barrier to growth. A more likely explanation is an intrinsic difference in kinetics between iron-bearing olivine and magnesium end-member forsterite. This is supported by the diffusion rates D_{Mg} in pure forsterite that are much slower and activation energies that are much higher compared to rates in Fe-bearing olivine (e.g. Chakraborty, 2010) in relation with different mechanisms of diffusion.

3.3. Implications for attenuation in the mantle transition zone

As they propagate through the Earth, seismic waves experience attenuation and dispersion attributed to solid state anelastic/viscoelastic relaxation. These dissipative effects can be summarized by the macroscopic quantity $Q^{-1} = -\Delta E/2\pi E_{\max}$, where ΔE is the internal energy lost by a seismic wave in one cycle. This quantity can be related to the often-used quality factor Q measured by seismologists. Relatively few 1D Q-profiles (Dziewonski and Anderson, 1981; Okal and Jo, 1990; Widmer et al., 1991; Durek and Ekström, 1996; Hwang and Ritsema, 2011; Durand et al., 2013) have been proposed over the last three decades owing to difficulties to isolate the intrinsic attenuation from the damping in seismic amplitudes due to scattering of the elastic wave (see review by Romanowicz and Mitchell, 2007). These models share several common features: the shear attenuation Q_μ^{-1} dominates the attenuation of the mantle, Q_μ^{-1} is high in the asthenosphere and decreases with depth, while the bulk attenuation Q_{K}^{-1} is much smaller. This attenuation can result from a diversity of petrological and mineralogical processes among which the motion of point defects and dislocations, grain boundary migration and sliding, the stress-induced redistribution of an intergranular fluid/melt phase, and volume strain associated with phase transformations (e.g. Jackson, 2007). Despite a large amount of experimental and theoretical works we are still far from understanding the contribution of each process to the observed seismic attenuation. Among the above mechanisms, solid–solid phase transformations may play an important role if the stress-induced changes in the proportions of coexisting phases were to result in relaxation of the bulk modulus within the seismic frequency band. The crucial issue is thus the timescale for the system undergoing phase transitions to reach equilibrium, in comparison with the period of seismic waves. For the olivine–wadsleyite transformation at the 410 km discontinuity two different models have been proposed to evaluate this characteristic time: (i) the diffusion-controlled growth

(Li and Weidner, 2008; Weidner and Li, 2010; Li, 2010), and (*ii*) interface-controlled growth models (Ricard et al., 2009). In the diffusion model the reaction time is controlled by the exchange of Mg–Fe species between olivine and wadsleyite through diffusion, while in the interface-controlled model the rate limiting step is the mobility of the olivine – wadsleyite interface. In both models nucleation is considered instantaneous since both phases already coexist in the binary loop. The two models conclude for a contribution of interface attenuation in 1D seismological models, but differ in the amount and frequency dependence of this attenuation. In the present work, we use the interface-controlled model of Ricard et al. (2009) since it is in agreement with our experimental observations of a pseudo-martensitic reaction mechanism, where the transition of olivine to ringwoodite operates by a shear-induced anionic rearrangement (i.e. motion of the interface) followed by a short-range diffusion of cations.

The thermomechanical model of Ricard et al. (2009) describes the equilibrium loop of a divariant solid–solid phase transformation involving both bulk and shear deformations. It shows that the resulting medium has a standard linear solid viscoelastic behaviour whose attenuation depends upon on the timescale of the transformation process. In Ricard et al. (2009), the stress perturbation ($\delta\sigma_n$) associated to a seismic wave induces a motion of the interface (ν) between the low and high-pressure phases with a linear kinetics:

$$[\nu] = C \cdot \delta\sigma_n = \frac{R_e}{\tau \cdot K_\infty}\delta\sigma_n \tag{5}$$

where the kinetic constant C is expressed as a function of R_e a typical grain size, K_∞ the high-frequency (unrelaxed) incompressibility, and τ a kinetic time constant. If the reaction occurs within the period of the seismic wave, the resulting attenuation within the transformation loop is given by:

$$Q^{-1} = \frac{(K_\infty - K_i)\omega\tau}{K_i + \omega^2\tau^2 K_\infty} \tag{6}$$

where K_i is the relaxed compressibility (i.e. relaxed with respect to the short timescale of seismic waves), and ω the frequency of the wave. This expression holds either for bulk (Q_K^{-1}) and shear (Q_μ^{-1}) attenuation using the kinetic characteristic time $\tau_\mu = 0.6\tau$ and $\tau_K = 0.4\tau$, respectively. For a more detailed description of the model, the reader is referred to Ricard et al. (2009) and Durand et al. (2012).

In this section we use the present kinetic data on the olivine transformation into the model of Ricard et al. (2009) in order to investigate the contribution of this phase change in the seismic attenuation of the mantle transition zone. The transformation rate for the olivine–wadsleyite transition in $(Mg_{0.9},Fe_{0.1})_2SiO_4$ is calculated from equation (4), assuming that nucleation does not affect the kinetics since the two phases are already present in the loop. The kinetic constant C, which is expressed in $m\,s^{-1}\,GPa^{-1}$, can be directly related to the growth rate (G) according to the relation $C \approx G.\Delta P$ with $\Delta P = 1$ GPa, assuming linearity between interface velocity and pressure perturbation. For mantle conditions of 13.5 GPa, geotherm temperature $T = 1600$ K and mantle olivine composition $X_{Fa} = 0.1$, the reaction rate (G) is estimated to 3.93×10^{-8} $m\,s^{-1}$ leading to a characteristic time $\tau = 1410$ s for a grain diameter of 1 cm. The bulk and shear attenuations at the centre of the loop are then computed as a function of period using equation (6), considering $K_\infty = 180$ GPa, $\mu_\infty = 85$ GPa (i.e. from PREM model at ~410 km depth) and mean values in the loop $K_i \approx 100$ GPa and $\mu_i \approx 50$ GPa. Fig. 7 compares the attenuation within the transformation loop with upper mantle PREM values (Dziewonski and Anderson, 1981). Except for the short period S waves, the predicted Q_K^{-1} and Q_μ^{-1} are significantly higher than the PREM values for both body waves and normal modes. Hence,

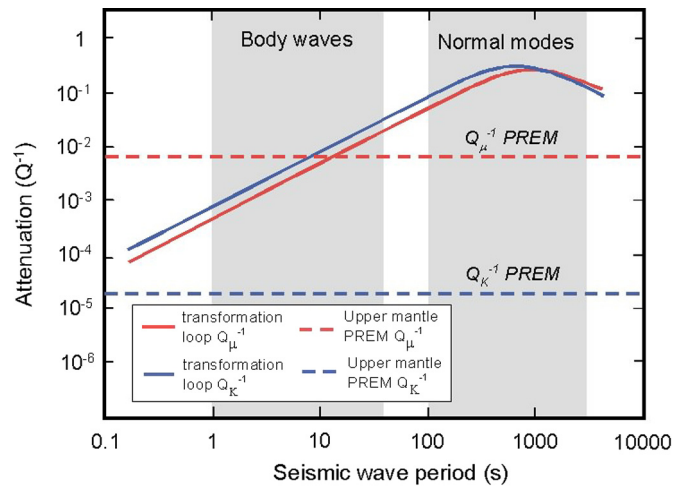

Fig. 7. Bulk (Q_K^{-1}) and shear (Q_μ^{-1}) attenuations at the centre of the loop computed as a function of period using equation (6). PREM upper-mantle values are shown by dashed lines. The typical period ranges of body waves and normal modes are shaded in light grey. The transformation loop potentially affects both P and S waves attenuation (except low period S waves) as well as normal modes.

the α–β transformation can significantly contribute to the bulk and shear attenuation of the Earth's upper mantle, though the narrow depth range of the loop may make this localized attenuation difficult to detect. This conclusion is in agreement with previous studies of Li and Weidner (2008) and Ricard et al. (2009) that stressed the contribution of interface attenuation in 1D seismological models. This does not imply that accounting for interface attenuation in seismological models would necessary significantly improve the fit with observations of Earth's attenuation. However this suggests that attenuation at the 410 km from olivine–wadsleyite transformation is a relevant dissipative process, and must be considered in further modelling of mantle seismic attenuation.

Durand et al. (2012) explored the range of characteristic time τ compatible with normal mode attenuation and body wave reflection coefficients, for a given thickness of the 410 km transition (see Fig. 8 in Durand et al., 2012). According to their predictions, the present kinetic time $\tau = 1410$ s (calculated for a grain size of 1 cm) would imply a thickness of the α–β transition of ~2 km that is indeed consistent with the lower bound of mineralogical and seismic estimates (e.g. Shearer, 2000). Finally, several seismic studies of the PP precursors (seismic waves that form from underside reflections of P waves off discontinuities in the upper mantle transition zone) reported weak amplitudes, and in some cases the non-detection, of these phases even in the presence of well-defined PP waveforms (e.g. Lessing et al., 2015). Attenuation due to the olivine α–β transformation in the transition zone may be responsible for the decrease precursor amplitudes relative to PP wave since the attenuation of PP precursors will be maximal near the reflection point at 410 km. This could provide a worldwide explanation for the difficulties to detect PP precursors.

3.4. Conclusions

We have determined the kinetics of the olivine–ringwoodite transformation for iron-rich compositions Fa52 and Fa66 using time-resolved X-ray diffraction in the range 6.8–10.7 GPa and 891–1172 K. Time series of XRD spectra reveal a transient amorphization of olivine at the onset of transformation consistent with the pseudo-martensitic reaction mechanism. Both microstructural and kinetic data suggest that the transformation rates are controlled by growth processes after the early saturation of nucleation sites along olivine grain boundaries. Growth rates in the range 1.13×10^{-10} $m\,s^{-1}$ to 5.51×10^{-9} $m\,s^{-1}$ are estimated by

fitting the transformation-time data to the Cahn rate equation, and show an exponential increase with temperature and iron content. Combining these results with previous data obtained on Fa10 samples (Perrillat et al., 2013), we propose a rate equation $G = k_0 \cdot T \cdot \exp[n \cdot X_{\mathrm{Fa}}] \cdot \exp[-(\Delta H_a + PV^*)/RT] \times [1 - \exp(\Delta G_r/RT)]$, where X_{Fa} is the fayalite fraction, the exponential factor $n = 9.7$, $\ln k_0 = -9.1\ \mathrm{m\,s^{-1}}$. X_{Fa}^{-1} and $\Delta H_a = 199$ kJ/mol, assuming $V^* = 0\ \mathrm{cm^3/mol}$.

These new kinetic results are included in the mechanical model of a two-phase loop of Ricard et al. (2009) to estimate the contribution of the olivine–ringwoodite phase change in the seismic attenuation of the mantle transition zone. Except for the short period S waves, the predicted Q_K^{-1} and Q_μ^{-1} are significantly higher than the PREM values for both body waves and normal modes, and confirmed the contribution of interface attenuation in 1D seismological models. Other mantle phase transformations like the post-spinel and post-garnet reactions should behave similarly; however estimation of their relaxation times requires the knowledge of their kinetics, which are at present largely unconstrained. Finally, we also propose that this localized attenuation in the transition zone may lower the amplitude of PP precursors $P^{410}P$, and may contribute to the well-known difficulties to detect PP precursors relative to the PP wave.

Acknowledgements

We acknowledge the European Synchrotron Radiation Facility for the allocation of synchrotron radiation beamtime. This work was supported by the CNRS – Institut National des Sciences de l'Univers, and the ANR project SEISGLOB ANR-11-BS56-0016. Electron microscopy in Lyon is supported by the Centre Lyonnais de Microscopie.

References

Akaogi, M., Ito, E., Navrotsky, A., 1989. Olivine–modified spinel–spinel transitions in the system Mg_2SiO_4–Fe_2SiO_4: calorimetric measurements, thermochemical calculations, and geophysical application. J. Geophys. Res. 94 (B11), 15671–15685.

Brearley, A.J., Rubie, D.C., Ito, E., 1992. Mechanisms of the transformations between the α, β and γ polymorphs of Mg_2SiO_4 at 15 GPa. Phys. Chem. Miner. 18, 18343–18358.

Burnley, P.C., 1995. The fate of olivine in subducting slabs: a reconnaissance study. Am. Mineral. 80, 1293–1301.

Cahn, J.W., 1956. The kinetics of grain boundary nucleated reactions. Acta Metall. 4, 449–459.

Chakraborty, S., 2010. Diffusion coefficients in olivine, wadsleyite and ringwoodite. Rev. Min. Petrol. 72, 603–639.

Chen, J., Weidner, D.J., Parise, J.B., Vaughan, M.T., Raterron, P., 2001. Observation of cation reordering during the olivine–spinel transition in fayalite by in situ synchrotron X-ray diffraction at high pressure and temperature. Phys. Rev. Lett. 86 (18), 4072–4075.

Diedrich, T., Sharp, T.G., Leinenweber, K., Holloway, J.R., 2009. The effect of small amounts of H_2O on olivine to ringwoodite transformation growth rates and implications for subduction of metastable olivine. Chem. Geol. 262, 87–99.

Du Frane, W.L., Sharp, T.G., Mosenfelder, J.L., Leinenweber, K., 2013. Ringwoodite growth rates from olivine with ∼75 ppm H_2O: metastable olivine must be nearly anhydrous to exist in the mantle transition zone. Phys. Earth Planet. Inter. 129, 1–10.

Durand, S., Matas, J., Ford, S., Ricard, Y., Romanowicz, B., Montagner, J.P., 2013. Insights from ScS–S measurements on deep mantle attenuation. Earth Planet. Sci. Lett. 374, 101–110. http://dx.doi.org/10.1016/j.epsl.2013.05.026.

Durand, S., Chambat, F., Matas, J., Ricard, Y., 2012. Constraining the kinetics of mantle phase changes with seismic data. Geophys. J. Int. 189, 1557–1564. http://dx.doi.org/10.1111/j.1365-246X.2012.05417.x.

Durek, J.J., Ekström, G., 1996. A radial model of anelasticity consistent with long period surface wave attenuation. Bull. Seismol. Soc. Am. 86, 144–158.

Dziewonski, A.M., Anderson, D.L., 1981. Preliminary reference Earth model. Phys. Earth Planet. Inter. 25, 297–356.

Furnish, M.D., Basset, W.A., 1983. Investigation of the mechanism of the olivine–spinel transition in fayalite by synchrotron radiation. J. Geophys. Res. 88, 10333–10341.

Green, H.W., Burnley, P.C., 1989. A new self-organizing mechanism for deep-focus earthquakes. Nature 341, 733–737.

de Groot, S.R., Mazur, P., 1984. Non-Equilibrium Thermodynamics. Dover Publications, New York.

Guyot, F., Gwanmesia, G.B., Liebermann, R.C., 1991. An olivine to beta phase transformation mechanism in Mg_2SiO_4. Geophys. Res. Lett. 18 (1), 89–92.

Hosoya, T., Kubo, T., Ohtani, E., Sano, A., Funakoshi, K., 2005. Water controls the fields of metastable olivine in cold subducting slabs. Geophys. Res. Lett. 32 (17), L17305.

Hwang, Y.K., Ritsema, J., 2011. Radial Q_μ structure of the lower mantle from teleseismic body-wave spectra. Earth Planet. Sci. Lett. 303, 369–375.

Jackson, I., 2007. Properties of rocks and minerals – physical origins of anelasticity and attenuation in rock. In: Schubert, G. (Ed.), Treatise in Geophysics. Elsevier.

Jacobs, M.H.G., de Jong, B.H.W.S., 2005. An investigation into thermodynamic consistency of data for the olivine, wadsleyite and ringwoodite form of $(Mg, Fe)_2SiO_4$. Geochim. Cosmochim. Acta 69 (17), 4361–4375.

Kerschhofer, L., Sharp, T.G., Rubie, D.C., 1996. Intracrystalline transformation of olivine to wadsleyite and ringwoodite under subduction zone conditions. Science 274, 79–81.

Kerschhofer, L., Rubie, D.C., Sharp, T.G., McConnell, J.D.C., Dupas-Bruzek, C., 2000. Kinetics of intracrystalline olivine–ringwoodite transformation. Phys. Earth Planet. Inter. 121, 59–76.

Kubo, T., Ohtani, E., Kato, T., Morishima, T., Yamakazi, D., Suzuki, A., Mibe, K., Kikegawa, T., Shimomura, O., 1998a. An in situ X ray diffraction study of the α–β transformation kinetics of Mg_2SiO_4. Geophys. Res. Lett. 25, 695–698.

Kubo, T., Ohtani, E., Kato, T., Shinmei, T., Fujino, K., 1998b. Effects of water on the α–β transformation kinetics in San Carlos olivine. Science 281, 85–87.

Kubo, T., Ohtani, E., Funakoshi, K., 2004. Nucleation and growth kinetics of the α–β transformation in Mg_2SiO_4 determined by in situ synchrotron powder X-ray diffraction. Am. Mineral. 89, 285–293.

Larson, A.C., Von Dreele, R.B., 2004. General Structure Analysis System (GSAS). Los Alamos National Laboratory report LAUR 86-748.

Lessing, S., Thomas, C., Saki, M., Schmerr, N., Vanacore, E., 2015. On the difficulties of detecting PP precursors. Geophys. J. Int. 201, 1666–1681. http://dx.doi.org/10.1093/gji/ggv105.

Li, L., Weidner, D.J., 2008. Effect of phase transitions on compressional-wave velocities in the Earth's mantle. Nature 454, 984–986.

Li, L., 2010. Bulk attenuation in the Earth's mantle due to phase transitions. Phys. Earth Planet. Inter. 183 (3–4), 473–477.

Libowitzky, E., Rossman, G.R., 1997. An IR absorption calibration for water in minerals. Am. Mineral. 82, 1111–1115.

Liu, M., Kerschhofer, L., Mosenfelder, J.L., Rubie, D.C., 1998. The effect of strain energy on growth rates during the olivine–spinel transformation and implications for olivine metastability in subducting slabs. J. Geophys. Res. 103, 23897–23909.

Matas, J., 1999. Modélisation thermochimique des propriétés de solides à hautes températures et hautes pressions. PhD thesis. Ecole Normale Supérieure de Lyon, Lyon, France.

Morard, G., Mezouar, M., Rey, N., Poloni, R., Merlen, A., Le Floch, S., Toulemonde, P., Pascarelli, S., San-Miguel, A., Sanloup, C., Fiquet, G., 2007. Optimization of Paris–Edinburgh press cell assemblies for in situ monochromatic X-ray diffraction and X-ray absorption. High Press. Res. 27 (2), 1–11.

Morard, G., Mezouar, M., Bauchau, S., Alvarez-Murga, M., Hodeau, J.L., Garbarino, G., 2011. High efficiency multichannel collimator for structural studies of liquids and low-Z materials at high pressures and temperatures. Rev. Sci. Instrum. 82, 023904.

Mosenfelder, J.L., Marton, F.C., Ross II, R.C., Kerschhofer, L., Rubie, D.C., 2001. Experimental constraints on the depth of olivine metastability in subducting lithosphere. Phys. Earth Planet. Inter. 127, 165–180.

Okal, E.A., Jo, B.G., 1990. Q measurements for phase X overtones. Pure Appl. Geophys. 132, 331–362.

Perrillat, J.P., Daniel, I., Bolfan-Casanova, N., Chollet, M., Morard, G., Mezouar, M., 2013. Mechanism and kinetics of the α–β transition in San Carlos olivine $Mg_{1.8}Fe_{0.2}SiO_4$. J. Geophys. Res. 118, 1–10. http://dx.doi.org/10.1002/jgrb.50061.

Poirier, J.P., 1981. On the kinetics of olivine–spinel transition. Phys. Earth Planet. Inter. 26, 179–187.

Raterron, P., Chen, J., Weidner, D.J., 2002. A process for low-temperature olivine–spinel transition under quasi-hydrostatic stress. Geophys. Res. Lett. 29, 101401. http://dx.doi.org/10.1029/2002GL015003.

Ricard, Y., Matas, J., Chambat, F., 2009. Seismic attenuation in a phase change coexistence loop. Phys. Earth Planet. Inter. 176, 124–131.

Romanowicz, B., Mitchell, B., 2007. Q in the Earth from crust to core. In: Schubert, G. (Ed.), Treatise of Geophysics. Elsevier.

Rubie, D.C., Ross II, C.R., 1994. Kinetics of the olivine–spinel transformation in subducting lithosphere: experimental constraints and implications for deep slab processes. Phys. Earth Planet. Inter. 86, 223–241.

Shearer, P.M., 2000. Upper mantle seismic discontinuities. In: Karato, S., et al. (Eds.), Earth's Deep Interior: Mineral Physics and Tomography from the Atomic to Global Scale. In: Geophys. Monogr., vol. 117. AGU, Washington DC, pp. 115–131.

Singh, A.K., Kennedy, G.C., 1974. Uniaxial stress component in tungsten carbide anvil high-pressure X-ray cameras. J. Appl. Phys. 45, 4686.

Smyth, J.R., Miyajima, N., Huss, G.R., Hellebrand, E., Rubie, D.C., Frost, D.J., 2012. Olivine–wadsleyite–pyroxene topotaxy: evidence for coherent nucleation and

diffusion-controlled growth at the 410-km discontinuity. Phys. Earth Planet. Inter. 200–201, 85–91.

Takemura, K., 2001. Evaluation of the hydrostaticity of a helium-pressure medium with powder X-ray diffraction techniques. J. Appl. Phys. 89 (1), 662–668.

Turnbull, D., 1956. Phase changes. Solid State Phys. 3, 225–306.

Weidner, D.J., Li, L., 2010. Impact of phase transitions on P wave velocities. Phys. Earth Planet. Inter. 180, 189–194.

Widmer, R., Masters, G., Gilbert, F., 1991. Spherically symmetric attenuation within the Earth from normal mode data. Geophys. J. Int. 104, 541–553.

Yagi, T., Akaogi, M., Shimomura, O., Suzuki, T., Akimoto, S.-I., 1987. In situ observation of the olivine–spinel phase transformation in Fe_2SiO_4 using synchrotron radiation. J. Geophys. Res. 92 (B7), 6207–6213.

Yamamoto, S., Ohno, I., Anderson, D.L., 1987. High temperature elasticity of sodium chloride. J. Phys. Chem. Solids 48 (2), 143–151.

Please cite this article in press as: Perrillat, J.P., et al. Kinetics of the olivine–ringwoodite transformation and seismic attenuation in the Earth's mantle transition zone. Earth Planet. Sci. Lett. (2015), http://dx.doi.org/10.1016/j.epsl.2015.11.013